Phonons and low thermal expansion in sodalite zinc borate $Zn_4B_6O_{12}X$ (X = O, S, Se)

Zhongsheng Wei,[1,*] Xingxing Jiang,[2,*] Anthony E. Phillips,[1] Zheshuai Lin,[2,†] and Martin T. Dove[3,4,5,1,‡]

[1]*School of Physical and Chemical Sciences, Queen Mary University of London, Mile End Road, London E1 4NS, United Kingdom*

[2]*Key Laboratory of Functional Crystals and Laser Technology of the Chinese Academy of Sciences, Technical Institute of Physics and Chemistry, Chinese Academy of Sciences, Beijing 100190, China*

[3]*College of Computer Science, Sichuan University, Chengdu 610065, China*

[4]*Department of Physics, School of Sciences, Wuhan University of Technology, 205 Luoshi Road, Hongshan district, Wuhan, Hubei 430070, China*

[5]*School of Mechanical Engineering, Dongguan University of Technology, 1st Daxue Road, Songshan Lake, Dongguan, Guangdong 523000, China*

(Received 25 October 2021; accepted 15 November 2021; published 29 November 2021)

We examine isotropic near-zero thermal expansion in the cubic materials $Zn_4B_6O_{12}X$ (X = O, S, Se) using density functional theory calculations of the lattice dynamics within the Grüneisen approximation. The calculated thermal expansion is in excellent agreement with experiment. The near-zero thermal expansion is shown to arise from a balance between two specific groups of vibrations that favor positive and negative thermal expansion, respectively. This gives a clear general indicator of how crystal structures can be engineered to give near-zero thermal expansion.

DOI: 10.1103/PhysRevB.104.174310

I. INTRODUCTION

In applications where materials face large temperature changes or temperature gradients, thermal expansion can cause many problems; ideally, such materials would have a coefficient of thermal expansion of zero [1–4]. While unusual, this behavior is not thermodynamically impossible. In our common experience, the volume of a solid will usually increase with temperature, for reasons that can be understood intuitively. Increasing volume will cause atoms to become slightly further apart, which will reduce the size of their harmonic force constants and lead to lower phonon frequencies and hence higher phonon entropy. In the overall free energy, the increase in energy associated with lattice expansion is favorably offset by the increased negative entropic contribution to the free energy. Given that this balance is controlled by temperature, higher temperatures lead to higher volume. Recently it has been found that some materials have the opposite behavior in that they shrink with increasing temperature, which is called "negative thermal expansion" (NTE) [5–12].

In fact, the phenomenon of near-ZTE is relatively rare, even rarer than NTE. Intrinsic near-ZTE has been found in a small number of materials, such as $CaMn_7O_{12}$ [13], $SrRuO_3$ [14], $Fe[Co(CN)_6]$ [15], $Mn_3Cu_{0.5}Ge_{0.5}N$ [16], TaO_2F [17], $N(CH_3)_4CuZn(CN)_4$ [18], YbGaGe [19], and $ZrMgMo_3O_{12}$ [20]. On the other hand, near-ZTE has been engineered by chemical doping in materials such as $PbTiO_3$ solid solutions [21,22], doped ScF_3 [23,24], $SrCu_3Fe_{4-x}Mn_xO_{12}$ [25], and $La(Fe,Si)_{13}$ hydrides [26]. Near-ZTE has also been generated in mesoporous $PbTiO_3$ fibers [27,28].

In this paper we will examine the theoretical basis for the existence of near-ZTE for temperatures below 300 K in the new framework material $Zn_4B_6O_{12}X$, where X represents O, S, or Se [29,30]. Our key finding is that near-ZTE materials can be designed by combining structural motifs that favor NTE with other motifs that have an opposing role.

In many cases, and of relevance in this paper, NTE arises from the existence of low-frequency vibrations involving the swinging motion of stiff bonds, a process known as the "tension effect." This has been described in several review articles [5,8,11], and arises because rotations of connected pairs of bonds pull the connected atoms inwards in preference to the stretching of the bonds. As temperature is increased, there will be larger amplitudes of the swinging motion, causing an increased inward pull that manifests as NTE. The role of the tension effect has been quantified in experimental and theoretical studies, as we have reviewed [31]. More recently the tension effect in ScF_3, as a pertinent example, was examined in detail by neutron total scattering and simulation [32].

The tension effect might be expected to be relevant to near-ZTE materials also, because it is expected that the local bonds will show positive thermal expansion in the same way that they do in NTE materials [32]. Thus in near-ZTE materials it might be expected that there is a fine balance between tension effect motions giving a negative contribution to thermal expansion and the positive thermal expansion of local bonds. This balance can, in principle, be tuned by crystal engineering. And the case of $Zn_4B_6O_{12}X$ is found here to illustrate how such engineering might be achieved in practice, mixing structural elements in a way that gives a near-perfect balance between these motions.

*Joint first author.
†zslin@mail.ipc.ac.cn
‡martin.dove@icloud.com

 ©2021 American Physical Society

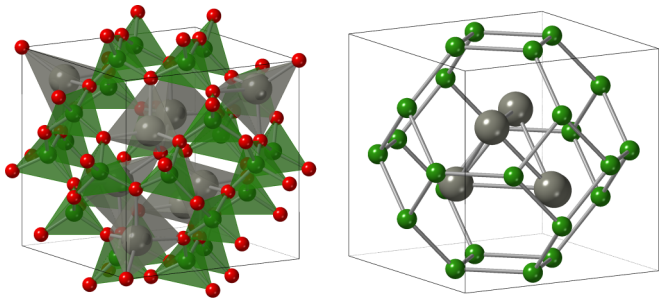

(a) Polyhedral view (b) Cation network

FIG. 1. Crystal structure of $Zn_4B_6O_{12}X$, cubic space group $I\bar{4}3m$ [33]. (a) The view shows the BO_4 (green) and ZnO_4 (gray) tetrahedra, with oxygen atoms shown as red spheres. (b) This shows the connectivity of tetrahedral centers, showing the sodalite network formed by the boron atoms (green), and the group of four zinc atoms occupying the centers of the sodalite cages (gray).

II. BACKGROUND CONCEPTS AND METHODOLOGY

A. The crystal structure of $Zn_4B_6O_{12}X$

This family of borates, with general formula of $Zn_4B_6O_{12}X$ (X = O, S, Se) and denoted ZBX, has a sodalitelike crystal structure [34]. The unit cell, with space group $I\bar{4}3m$ [33], is shown in Fig. 1. The characteristic feature of the sodalite structure is a cubic-symmetrical cage consisting of TO_4 tetrahedra (T = Al, Si, Be, B, P) [35,36], which are shown as green in Fig. 1(a). The topology of the sodalite cage, forming a truncated octahedron, is shown in Fig. 1(b), where we show the network of neighboring tetrahedral sites. The cage consists of eight rings of six connected tetrahedra, which are parallel to the set of {111} planes. These rings are joined together to form square rings of four tetrahedra, which are parallel to the set of {100} planes. These square rings are then connected to the corresponding rings in the adjacent unit cells to provide channels between the cages. In the crystal structure of $Zn_4B_6O_{12}X$, an XZn_4 tetrahedron occupies the center of each cage, with each Zn bonding to three O atoms to form a $ZnXO_3$ distorted tetrahedron. These tetrahedra are shown with gray color in Fig. 1(a), and the group of Zn sites within the cage is shown in Fig. 1(b).

The existence of near-ZTE in ZBX is likely to be related to the flexibility of the sodalitelike framework structure [37–39]. Several kinds of zeolites contain $[Si_{24}O_{48}]$ cages with sharing four-tetrahedra faces within their structures. Examples include zeolite A (LTA) and faujasite (FAU) [40], which display NTE over a wide range of temperature [41]. The strong NTE in zeolites arises from these zeolites supporting a spectrum of rigid unit modes (RUMs) which enable the tension effect. However, the case of the sodalite cages in ZBO, ZBS, and ZBSe is different, because the central XZn_4 tetrahedron can make the structure more rigid. This might be expected to give resistance to NTE, facilitating a balance between negative and positive thermal expansion and thereby giving rise to near-ZTE. It was this possibility that motivated the original work on this material [29,30], and indeed, this is exactly what is found in this paper. The conclusion from this study is that one route to developing near-ZTE materials by crystal engineering is to stiffen a material of known flexibility, such as one containing a network of tetrahedra. This can be done in such a way that the NTE vibrations are raised to higher frequency, and are then balanced by low-frequency modes giving positive thermal expansion, arising from the atomic clusters acting as cross braces.

B. Grüneisen model of thermal expansion

The coefficient of thermal expansion $\alpha_V = V^{-1}(\partial V/\partial T)_P$ is given by [11]

$$\alpha_V = \frac{\overline{\gamma} C_V}{BV}, \tag{1}$$

where C_V is the heat capacity, $B = -V(\partial P/\partial V)_T$ is the bulk modulus, V is the volume, and $\overline{\gamma} = -(\partial \ln T/\partial \ln V)_S$ is a dimensionless parameter known as the overall Grüneisen parameter [42–44].

In this paper we make use of the Grüneisen theory [44], which is based on a quasiharmonic model [8,11,45]. It is assumed that the normal theory of harmonic lattice dynamics can be used to calculate the phonon free energy of a given state of the crystal. Following a small expansion or contraction of the lattice, it is assumed that the harmonic phonon free energy will change due to changes in the interatomic force constants leading to small changes in phonon frequencies. These changes are quantified by the mode Grüneisen parameter:

$$\gamma_j = -\frac{V}{\omega_j}\frac{\partial \omega_j}{\partial V}, \tag{2}$$

where each phonon mode has label j. The overall Grüneisen parameter $\overline{\gamma}$ describes how on average the phonon frequencies change with volume. It can be obtained as a weighted mean of γ_j:

$$\overline{\gamma} = \frac{1}{C_V}\sum_j c_j \gamma_j, \tag{3}$$

where

$$c_j = \hbar\omega_j \frac{\partial n(\omega_j, T)}{\partial T} \tag{4}$$

and $n(\omega_j, T)$ is the Bose-Einstein distribution.

What is important in this formalism is that vibrations with positive values of mode Grüneisen parameter contribute to positive thermal expansion and those with negative values contribute to NTE. This will allow us to better understand the origin of near-ZTE through inspection of the balance between these two types of vibration.

It should be noted that the quasiharmonic approximation includes anharmonic effects in which force constants change with volume, but does not include the effects of frequency renormalization through anharmonic phonon-phonon interactions. While the quasiharmonic approximation is convenient for calculations, and is found to be generally reasonable, it is known that phonon-phonon anharmonic effects tend to cause NTE to become less negative—and in some cases make it become positive—at high temperature. This has been explored theoretically in model systems [46], and in the specific case of ScF_3 [47]. Thus, in this paper it is appropriate that our comparison between simulation and

experimental data is for temperatures below room temperature, where we expect the quasiharmonic approximation to be most valid.

C. Simulation methods

Our primary approach is to calculate the set of mode Grüneisen parameters from phonon calculations performed using density functional theory (DFT) methods and density-functional perturbation theory (DFPT) methods [48,49].

The DFT calculations were performed using the CASTEP program [50]. CASTEP uses plane-wave electronic basis sets, and in our calculations we used norm-conserving pseudopotentials using the NCP19 set supplied by CASTEP. In our calculations ZBO, ZBS and ZBSe were regarded as explicit insulators. Exchange and correlation energies were calculated by the PBE formulation of the generalized gradient approximation (GGA) [51,52]. Cut-off energies were set to 1200 eV, and a Monkhorst-Pack grid of $3 \times 3 \times 3$ wave vectors within the reciprocal unit cell was used; these limits were established by testing for convergence of the differences in energy between two structures of slightly different volume.

Phonon frequencies calculated using the DFPT method made use of the interpolation method, whereby the dynamical matrix is formulated on a regular grid of phonon wave vectors, so that the dynamical matrices for "arbitrary" wave vectors can be formed by interpolation. For calculations of mode Grüneisen parameters, calculations of phonon frequencies were performed for both a fully relaxed structure at zero pressure, and for a relaxed structure with a 1% expansion in each direction. In addition to calculating dispersion curves, we also computed frequencies for 10 000 random wave vectors in the Brillouin zone [53]. Results were analyzed using our own software for evaluation of mode Grüneisen parameters [54] as used in other similar studies [55,56].

III. RESULTS

A. Crystal structure relaxation

The results for our calculations of the crystal structure of the three ZBX phases are compared with experimental data obtained at a temperature of 5 K in Table I. It can be seen that the DFT calculation overestimates the lattice parameters by a maximum of 0.8%, which we consider to be reasonable and in line with common experience with GGA functionals. The largest difference between observed and calculated bond lengths is 1.6%, and in most cases the agreement is much better than this. We consider that the DFT calculations have reproduced the overall crystal structures reliably.

It is worth noting the effects of substitution of the X anion as seen in bond lengths (Table I) and bond angles. The effect of changing anion X is to increase the Zn$-X$ distance, by 14% in going from O to S, and in a further 5% in going from S to Se (from the simulation results), leading to the respective increases in lattice parameters of 2.0% and 0.8%, respectively. On the other hand, changes in the B–O bond length on substitution are only 0.3% for the largest substitution, which means that the local strain caused by substitution on the X site must be accommodated through a small buckling of the sodalite network. On the two substitutions, the O–B–O tetrahedral angle only deforms by a maximum of less that 1°. Instead, the buckling of the sodalite framework occurs through rigid tetrahedral rotations bending the B–O–B angles, with changes in the two substitutions of 4.5° and 1.3° for S and Se, respectively. This is consistent with the analysis of rigid unit modes (RUMs) within the sodalite structure. Analysis shows the existence of RUMs with zero wave vector that can cause buckling of the structure and lower the symmetry from the ideal space group $Im\bar{3}m$ to $I\bar{4}3m$ [37–39]. This will allow for the local strain to be accommodated within the sodalite structure easily, with little energy cost.

TABLE I. Comparison of experimental and calculated crystal properties of $Zn_4B_6O_{12}X$, where X = O, S, or Se. The crystal structure has space group $I\bar{4}3m$. Atomic coordinates are B (1/4, 1/2, 0), Zn (x, x, x), X (1/2, 1/2, 1/2), and O (x, x, z). Elastic constant data are from Ref. [29].

	$Zn_4B_6O_{13}$		$Zn_4B_6O_{12}S$		$Zn_4B_6O_{12}Se$	
	Expt.	Calc.	Expt.	Calc.	Expt.	Calc.
a (Å)	7.47	7.53	7.63	7.68	7.68	7.74
Zn x	0.346	0.347	0.328	0.329	0.322	0.322
O x	0.139	0.140	0.143	0.143	0.144	0.144
O z	0.414	0.416	0.425	0.426	0.430	0.429
B–O (Å)	1.477	1.482	1.480	1.487	1.474	1.489
Zn–O (Å)	1.952	1.984	1.954	1.980	1.972	1.980
Zn-X (Å)	1.987	2.000	2.273	2.279	2.369	2.386
C_{11} (GPa)	312.2	308.0	–	286.7	–	287.9
C_{12} (GPa)	137.6	124.9	–	124.9	–	124.0
C_{44} (GPa)	102.3	94.9	–	82.1	–	85.9
B (GPa)	195.8	185.9	–	178.9	–	178.6

B. Zone center optic phonons

The calculated phonon frequencies for zero wave vector for ZBO, corrected for longitudinal/transverse splitting of optical modes (LO/TO), are given in Table II. The mode decomposition for the acoustic modes is T_2, and for optic modes is $3A_1 + 2A_2 + 5E_1 + 7T_1 + 10T_2$. The T_2 modes show LO/TO splitting. The A_1, A_2, E_1, and T_2 modes are Raman active, and the T_2 modes are also IR active. The T_1 modes are inactive in both Raman and IR spectroscopy. Similar tables for ZBS and ZBSe are given as Tables S1 and S2 in the Supplemental Material (SM) [57].

In order to assess the validity of the phonon calculations, we have measured the vibrational frequencies by infrared (IR) spectroscopy to support previous measurements by Raman spectroscopy [30]. The IR and Raman spectra for all three samples of ZBX are given in Fig. S1 in the SM [57]. The experiments do not themselves help with the symmetry assignment of modes, and therefore the assignment of modes based solely on proximity of experimental frequencies to calculated values is only tentative. These are given for in Tables S3–S5 in the SM [57]. What we can deduce from these tentative assignments is that there are no obvious significant discrepancies between calculated and experimental mode frequencies.

TABLE II. Calculated vibration frequencies for zero wave vector for $Zn_4B_6O_{13}$. The symbols R and IR indicated Raman and infrared activity.

$3A_1$ (R)		$2A_2$ (R)		$5E_1$ (R)		$7T_1$ (–)		$10T_2$ (R,IR)			
								$10E_2$		$10B$	
(cm^{-1})	(THz)	(cm^{-1})	(THz)	(cm^{-1})	(THz)	(cm^{-1})	(THz)	(cm^{-1})	(THz)	(cm^{-1})	(THz)
240.4	7.22	414.1	12.44	172.3	5.17	139.7	4.20	172.7	5.19	173.2	5.20
404.1	12.14	856.8	25.73	399.8	12.01	280.2	8.41	188.7	5.67	215.7	6.48
706.9	21.23			697.2	20.94	434.8	13.06	263.5	7.91	270.7	8.13
				808.5	24.28	644.8	19.36	446.5	13.41	446.9	13.42
				1045.1	31.37	771.1	23.16	455.2	13.67	471.6	14.16
						878.9	26.39	627.8	18.85	628.0	18.86
						1034.1	31.05	693.3	20.82	708.1	21.26
								869.9	26.12	971.1	29.16
								999.8	30.02	1003.0	30.12
								1029.3	30.91	1132.8	34.02

C. Phonon dispersion curves and densities of states

The phonon dispersion curves of ZBO are shown in the left image of Fig. 2. Corresponding phonon dispersion curves for ZBS and ZBSe are given in the SM [57], Figs. S2 and S3. All three materials show very similar phonon dispersion curves.

From the gradients of the acoustic modes we have calculated the three elastic constants C_{11}, C_{12}, and C_{44}, which are given in Table I. For ZBO we are able to compare with experimental data [29], and the agreement is satisfactory. The calculated values are slightly lower than the experimental values, giving an overall underestimate of the calculated value of the bulk modulus $B = (C_{11} + 2C_{12})/3$ of 5% compared to the experimental value.

The phonon densities of states of all three materials are shown in Fig. 3. The densities of states are all very similar for frequencies of around 20 THz and above. Particular features are the sharp groups of peaks around 25 THz, the broader bands of modes around 30 THz with a final sharp peak at around 33 THz, and the broad bands of modest around 20 THz and above with first sharp peaks at around 18 THz. There are more general differences for lower frequencies on top of some similar features. In particular, a sharp peak appears at 15 THz in ZBO, at 10 THz in ZBS, and at 7 THz in ZBSe. It appears that at lower frequencies the density of states is more sensitive to the replacement of O by S and Se.

In order to interpret the vibrations in terms of atomic motions, we have analyzed the modes at zero wave vector for the

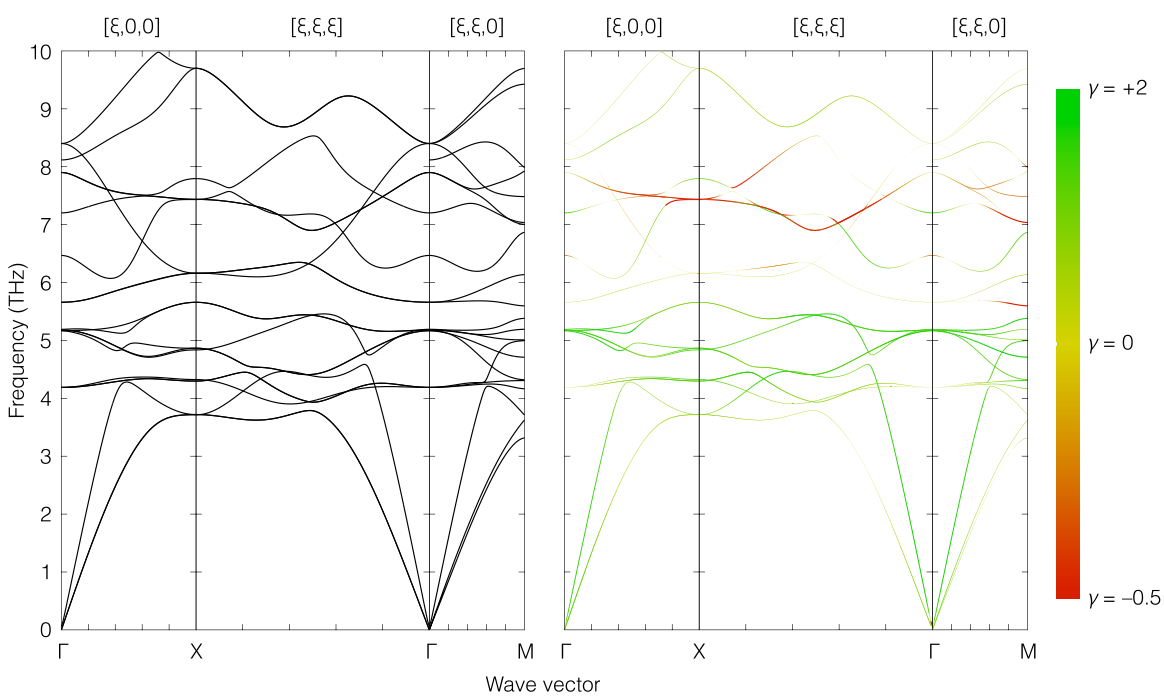

FIG. 2. Left, calculated phonon dispersion curves of $Zn_4B_6O_{13}$ for frequencies below 10 THz and for wave vectors along along symmetry directions in reciprocal space. The alphabetic labels denote wave vectors of high symmetry: $\Gamma = 0, 0, 0$, $X = 1, 0, 0 \equiv 1, 1, 1$, and $M = 1/2, 1/2, 0$. Right, the same dispersion curves colored according to the size of the corresponding mode Grüneisen parameters; yellow corresponds to $\gamma = 0$, deepest red corresponds to $\gamma \leqslant -0.5$, and bright green corresponds to $\gamma \geqslant +2.0$.

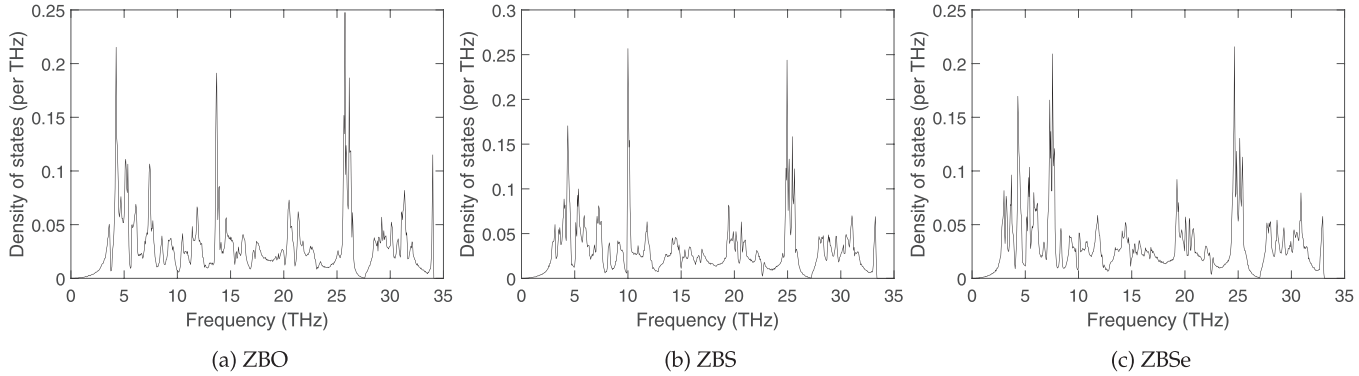

FIG. 3. Phonon density of states of the three materials (a) $Zn_4B_6O_{13}$, (b) $Zn_4B_6O_{12}S$, and (c) $Zn_4B_6O_{12}Se$.

three materials ZBX. The lattice dynamics calculations give orthonormal mode eigenvectors, which for each atom j is represented here as $\mathbf{e}_j$. Normalization means that $\sum_j |\mathbf{e}_j|^2 = 1$. We define atomic squared displacements as $u_j^2 = |\mathbf{e}_j|^2/m_j$, where m_j is the atomic mass of atom j [58,59]. We then sum the values of u^2 for each atom type in order to give the overall contribution from each atom type. These are plotted as a bar chart for each normal mode for the case ZBO in Fig. 4, together with a chart giving the frequency of each mode. For a check, for modes 1–3, which are the acoustic modes with zero frequency, we expect the values of u_j^2 to be equal for each atom, and hence the size of each contribution within the bars for these three modes will simply be proportional to the number of atoms of each type.

Figure 4 shows a number of features that will help us to understand the nature of vibrations. First we note that the vibrations involving significant contributions from Zn motion are in the frequency range around 0–5 THz, not surprising given the significant difference in mass between Zn and the B and O atoms. For modes with frequencies in the range 5–10 THz we see mostly O motions. These modes correspond to rotations of the BO_4 (and consequently of the ZnO_4 tetrahedra) and are the RUMs of the sodalite network. There is a sharp band of modes involving almost mostly the O(X) atom motions at around 13 THz, which is seen as the peak in the density of states of $Zn_4B_6O_{12}S$ in Fig. 3(a). Given the distance between X atoms in neighboring unit cells, any vibration involving mostly the X atom is unlikely to have high spatial correlation and so will represent effectively independent oscillators, giving the branch in the dispersion curve that is of almost constant frequency. This mode is seen to shift to lower frequencies in the corresponding plots in Figs. S4 and S5 in the SM [57], and is consistent with the shift in the peak in the phonon densities of states in Fig. 3. The higher-frequency modes involve mostly B and O atomic motions, and will represent B–O stretching and O–B–O bond-bending modes. The analysis of the higher-frequency modes shown in Fig. 4 for ZBO is well reproduced for ZBS and ZBSe.

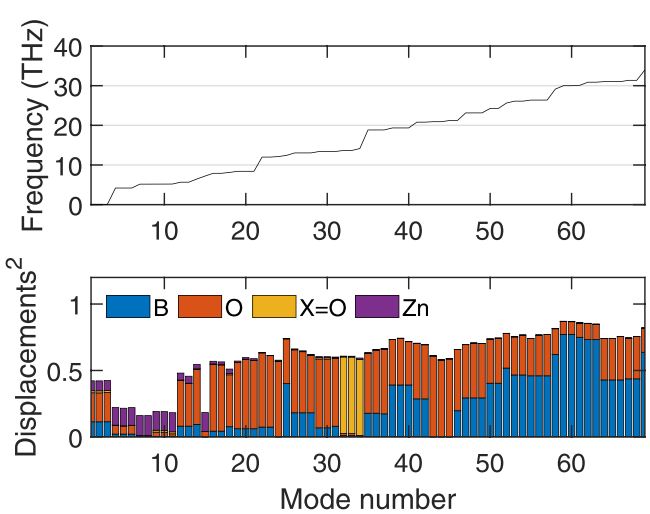

FIG. 4. The lower figure shows a bar chart showing decomposition of motions by atom type for the calculated lattice dynamics of ZBO. We label the abscissa in terms of mode number, and the the upper figure gives the corresponding mode frequency. The legend defines the atom type. Corresponding figures for ZBS and ZBSe are given in the SM, Figs. S4 and S5, respectively [57].

D. Evaluation of the mode Grüneisen parameters

Figure 2 (right-hand side) also shows the phonon dispersion curves of ZBO colored to display the values of the mode Grüneisen parameters of each branch Eq. (2) indicating by the color scheme whether the modes have positive or negative values of their Grüneisen parameters and hence whether the modes contribute to positive or negative thermal expansion. Corresponding images for X = S and Se are shown in Figs. S2 and S3. What can be seen from these colored dispersion curves is that it appears that the lower-frequency modes favor positive expansion, but with a band of modes around 7 THz that favor NTE.

More information can be obtained by averaging across the Brillouin zone from the calculations using sets of 10 000 random wave vectors. Figure 5 shows the distribution of values of mode Grüneisen parameters across the range of frequencies. It can be seen that in all three cases the distribution from 0–5 THz tends to prefer positive thermal expansion, and immediately above that the modes overall favor negative thermal expansion. From Fig. 4 we see that the lower frequency modes with positive values of the mode Grüneisen parameters are the modes with significant motions of the zinc atoms, and the modes with negative values of the mode Grüneisen parameters and frequencies just above 5 THz are the RUMs of the sodalite network. 5 THz corresponds to a temperature of 240 K, which

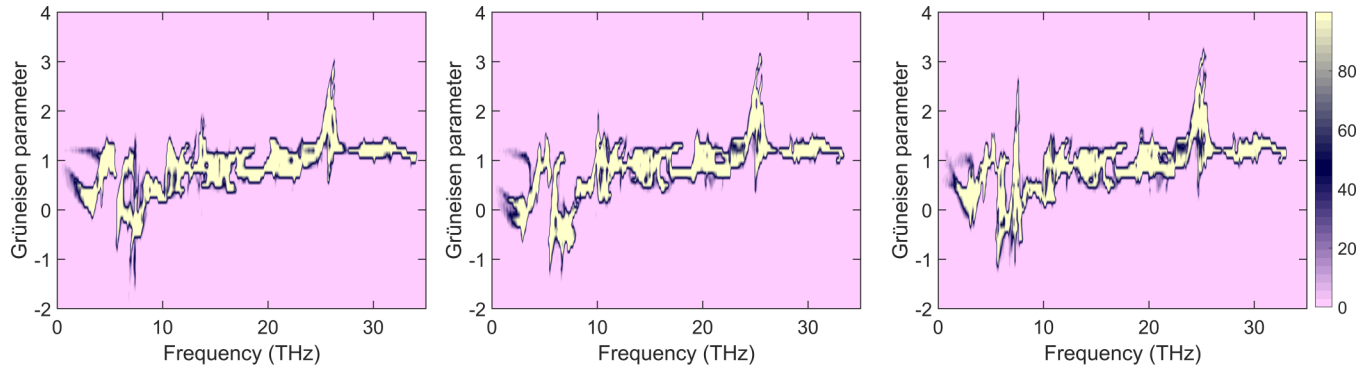

(a) ZBO (b) ZBS (c) ZBSe

FIG. 5. Color map of the distribution of mode Grüneisen parameters and mode frequencies of (a) $Zn_4B_6O_{13}$, (b) $Zn_4B_6O_{12}S$, and (c) $Zn_4B_6O_{12}Se$. The bar on the far right indicates how the colors represent the size of the distribution for any point on the map: pinks indicates complete absence of any modes with that pair of Grüneisen parameter and frequency. Yellow represents where the number of modes reaches a saturation maximum number (100 in a total number of 10 000). Dark blue represents intermediate numbers in the distribution.

means we expect to see the balance between positive and negative thermal expansion to be in play at temperatures below room temperature. However, there are some modes with negative values of γ within the 0–5 THz region, and the mean of the distribution is much lower than the value $\gamma \sim 1$ about which the higher-frequency modes are distributed.

This balance results in an interesting temperature dependence of the overall Grüneisen parameters $\overline{\gamma}$, as calculated using Eq. (3) and shown in Figs. 6(a)–6(c). At high temperatures, the values of $\overline{\gamma}$ tend to a limiting value of around 1, but at temperatures below room temperature $\overline{\gamma}$ falls as low as 0.52, 0.12, and 0.45 in ZBO, ZBS, and ZBSe, respectively. At low temperature we see that the balance between modes of positive and negative values of γ causes $\overline{\gamma}$ in ZBO to have two minima at lower temperatures. Although this is not seen in ZBS and ZBSe, there are points of inflection in the temperature dependencies of $\overline{\gamma}$ in these two materials which correspond to the second minimum seen in ZBO.

From calculations of $\overline{\gamma}$, the heat capacity calculated from the phonon frequencies via summation of c_j values of Eq. (4) (Fig. S6 in the SM [57]), and the bulk modulus values shown in Table I, we have computed the overall coefficient of volume

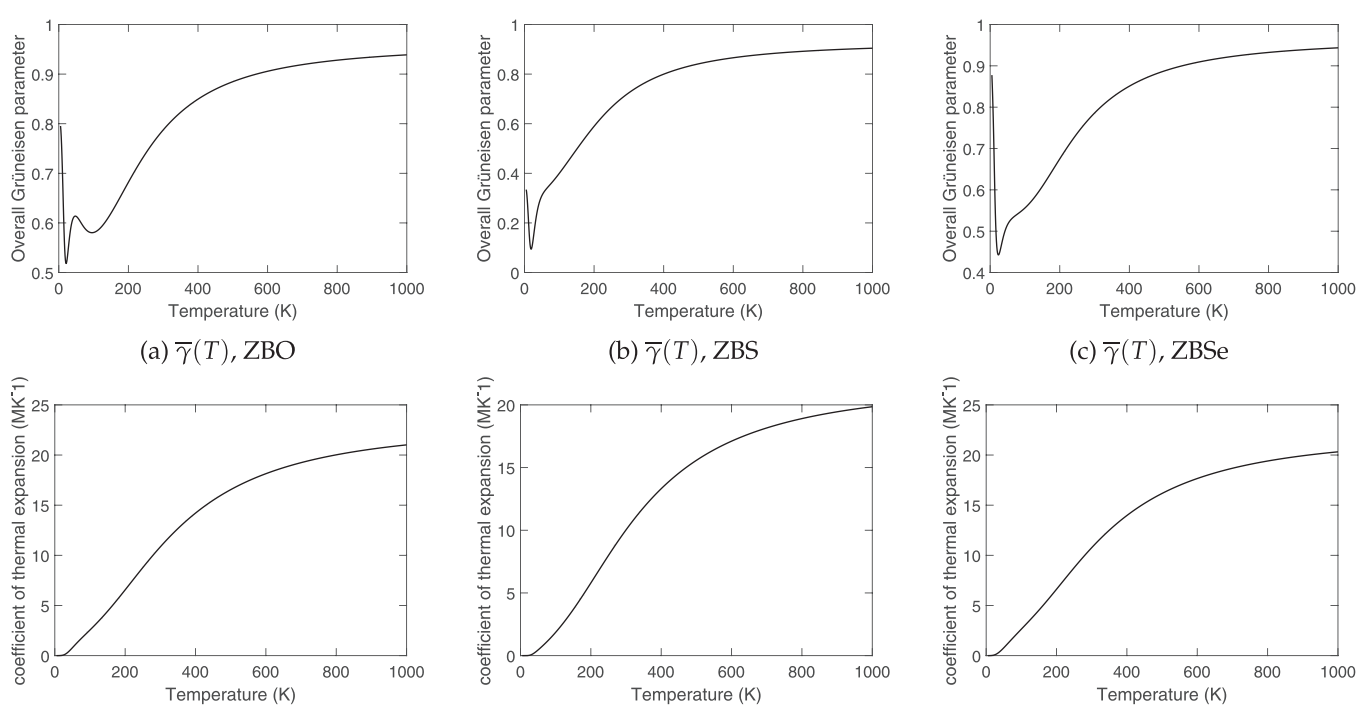

(a) $\overline{\gamma}(T)$, ZBO (b) $\overline{\gamma}(T)$, ZBS (c) $\overline{\gamma}(T)$, ZBSe

(d) $\alpha_V(T)$, ZBO (e) $\alpha_V(T)$, ZBS (f) $\alpha_V(T)$, ZBSe

FIG. 6. Top: Temperature dependence of the calculated overall Grüneisen parameters of $\overline{\gamma}$ of (a) $Zn_4B_6O_{13}$, (b) $Zn_4B_6O_{12}S$, and (c) $Zn_4B_6O_{12}Se$. Bottom: Temperature dependence of the calculated coefficient of volumetric thermal expansion α_V of (d) $Zn_4B_6O_{13}$, (e) $Zn_4B_6O_{12}S$, and (f) $Zn_4B_6O_{12}Se$.

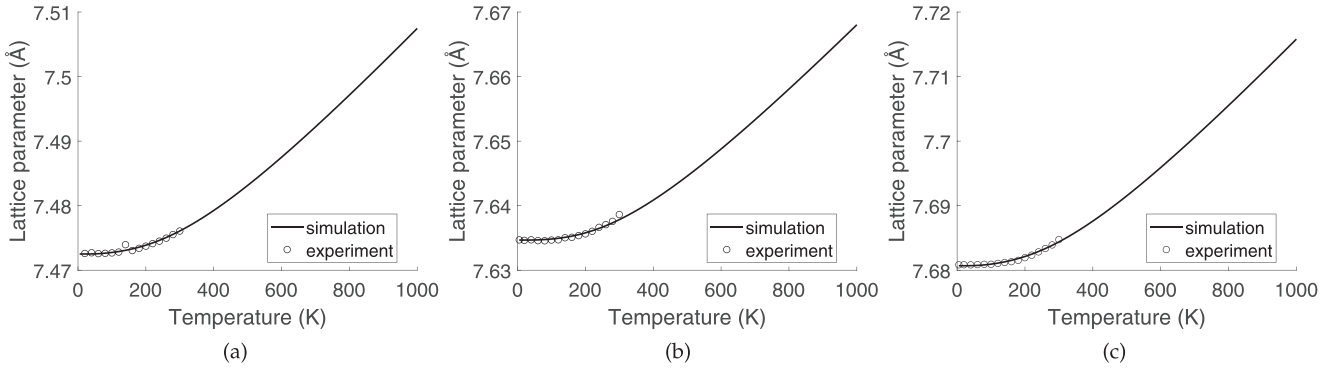

FIG. 7. Calculated lattice parameters of $Zn_4B_6O_{13}$, $Zn_4B_6O_{12}S$, and $Zn_4B_6O_{12}Se$ compared to experimental data. Circles corresponding to the experimental data [30], and black lines corresponding to the DFT simulation data. The DFT results have been shifted by values of −0.0582, −0.0522, and −0.0626 Å, respectively, to aid comparison of the thermal expansion.

thermal expansion α_V through Eq. (1). The results are shown in Figs. 6(d)–6(f). It should be noted that the value of the coefficient of linear expansivity, $\alpha_a = a^{-1}\partial a/\partial T$, is 1/3 of the value of α_V. From Fig. 6 it can be seen that the average value of $\alpha_V/3$ over the range 0–300 K is around 1.7 MK^{-1}, in line with the experimental results [30]. It is interesting to note that the minima in the temperature dependence of $\overline{\gamma}$ are not discernible in the values of α_V. This is because the rapidly rising heat capacity (varying as T^3 at first, Fig. S6 in the SM [57]) means that the overall form of α_V also rises too fast over the relevant range of temperatures for the effect of the variations in $\overline{\gamma}$ to be visible.

Finally, we have calculated the temperature dependencies of the lattice parameters of the three phases, which are shown in Fig. 7 and compared with experimental values [30]. We have shifted our calculations to bring the lowest temperature values into agreement to account for the DFT efforts (rather than simply compare scaled values). What can be seen is that in each of the three systems the agreement between calculation and experiment is excellent, with the calculations reproducing the low value of the linear thermal expansion over the temperature range 0–300 K [30].

IV. DISCUSSION

The gratifying result from the work presented in this paper is that the DFT calculations have reproduced the low thermal expansion in all three systems (ZBO, ZBS, and ZBSe) over the temperature range 0–300 K.

What is clear from the analysis is that the phonons at low frequencies (corresponding to temperatures below 300 K) have competing effects on the thermal expansion, giving rise to a relatively low values of the overall Grüneisen parameters in all these systems and hence low thermal expansivity for temperatures over the range 0–300 K. Only at higher temperatures, when the higher-frequency modes with values of mode Grüneisen parameters $\gamma \sim 1$, does the thermal expansivity increase to more usual values.

The origin of the low expansivity at lower temperatures, and existing over a wider range of temperatures than normal, comes from the competing contributions to the overall Grüneisen parameters up to relatively high frequency. The low-frequency modes have a low positive contribution to the expansivity, but over a range of around 5–8 THz the modes now compete to give lower values of the overall Grüneisen parameters. Only for frequencies above 10 THz, which corresponds to a temperature of 480 K, will the thermal expansivity have a more typical value. This is seen clearly in Fig. 6.

We believe that the origin of near-ZTE at low temperature in ZBO, ZBS, and ZBSe is related to the fact that the crystal structure is based on the sodalite structure. This structure is known to be flexible through the excitation of rigid unit modes (RUMs) [37–39,60]. It is know that zeolite structures based on the sodalite structure will give rise to NTE [41,61,62], and the RUM model provides a natural explanation for why the tension effect is able to be effective in a network structure [63,64]. Usually RUMs have low frequencies, but in the case of ZBX structures the central XZn_4 tetrahedron forming an overall rigid Zn_4XO_{12} unit makes the structure rigid. This raises the frequencies of the modes that would be RUMs, and means that the modes that contribute negatively to the thermal expansion now compete at higher energy with modes that contribute positively. Moreover, the higher frequencies of the RUM-like motions of the sodalite cage have reduced the values of the negative mode Grüneisen parameters as compared to those of the corresponding silica phases [11].

The competition between vibrations giving contributions to both positive and negative thermal expansivity may suggest routes towards the rational design of near-ZTE materials. In the case of ZBX materials, the key feature is that of taking a network structure that is known to show NTE and then making the network more rigid by cross bracing with additional atomic units. While this does not directly remove the effect of the vibrations that give NTE, it reduces the size of their effect by raising their frequency, and allows a balanced competition with other low-frequency modes that will contribute to positive expansivity. The example of ZBX therefore suggests a route towards the design of new near-ZTE materials.

ACKNOWLEDGMENTS

This research made use of the high-performance computing resources of the Midlands Plus Tier-2 HPC facility, funded by EPSRC Grant No. EP/P020232/1 (MTD). X.J. and Z.L. acknowledge financial support from the National Scientific Foundation of China (Grants No. 51872297, No. 51702330,

and No. 11974360). X.J. acknowledges the support from the Youth Innovation Promotion Association in CAS (Grant No. 017035) and Young Elite Scientist Sponsorship Program by CAST (Grant No. YESS20200149).

[1] I. J. K. Kim and H. Supkwak, Thermal shock resistance and thermal expansion behaviour with composition and microstructure of Al_2TiO_5 ceramics, Can. Metal. Q. **39**, 387 (2000).

[2] K. J. Yoon, H. C. Park, H. J. Lee, and C. K. Kim, Composite grid structure with near-zero thermally induced deflection, AIAA J. **39**, 487 (2001).

[3] K. Hosaka, H. Inaba, D. Akamatsu, M. Yasuda, J. Sugawara, A. Onae, and F.-L. Hong, A Fabry–Pérot etalon with an ultralow expansion ceramic spacer, Jpn. J. Appl. Phys. **52**, 032402 (2013).

[4] K. E. Hrdina and C. A. Duran, ULE® glass with improved thermal properties for EUVL masks and projection optics substrates, Int. J. Appl. Glass Sci. **5**, 82 (2014).

[5] A. W. Sleight, Compounds that contract on heating, Inorg. Chem. **37**, 2854 (1998).

[6] J. S. O. Evans, Negative thermal expansion materials, J. Chem. Soc. Dalton Trans. 3317 (1999), doi:10.1039/A904297K.

[7] C. Lind, Two decades of negative thermal expansion research: Where do we stand?, Materials **5**, 1125 (2012).

[8] G. D. Barrera, J. Bruno, T. Barron, and N. L. Allan, Negative thermal expansion, J. Phys.: Condens. Matter **17**, R217 (2005).

[9] W. Miller, C. W. Smith, D. S. Mackenzie, and K. E. Evans, Negative thermal expansion: A review, J. Mater. Sci. **44**, 5441 (2009).

[10] J. Chen, L. Hu, J. Deng, and X. Xing, Negative thermal expansion in functional materials: Controllable thermal expansion by chemical modifications, Chem. Soc. Rev. **44**, 3522 (2015).

[11] M. T. Dove and H. Fang, Negative thermal expansion and associated anomalous physical properties: Review of the lattice dynamics theoretical foundation, Rep. Prog. Phys. **79**, 066503 (2016).

[12] R. Mittal, M. K. Gupta, and S. L. Chaplot, Phonons and anomalous thermal expansion behaviour in crystalline solids, Prog. Mater. Sci. **92**, 360 (2018).

[13] O. Volkova, Y. Arango, N. Tristan, V. Kataev, E. Gudilin, D. Meier, T. Lorenz, B. Büchner, and A. Vasil'ev, Nature of low-temperature phase transitions in $CaMn_7O_{12}$, J. Exp. Theor. Phys. Lett. **82**, 444 (2005).

[14] T. Kiyama, K. Yoshimura, K. Kosuge, Y. Ikeda, and Y. Bando, Invar effect of $SrRuO_3$: Itinerant electron magnetism of Ru 4*d* electrons, Phys. Rev. B **54**, R756 (1996).

[15] S. Margadonna, K. Prassides, and A. N. Fitch, Zero thermal expansion in a Prussian Blue analogue, J. Am. Chem. Soc. **126**, 15390 (2004).

[16] X. Song, Z. Sun, Q. Huang, M. Rettenmayr, X. Liu, M. Seyring, G. Li, G. Rao, and F. Yin, Adjustable zero thermal expansion in antiperovskite manganese nitride, Adv. Mater. **23**, 4690 (2011).

[17] J. Tao and A. Sleight, Very low thermal expansion in TaO_2F, J. Solid State Chem. **173**, 45 (2003).

[18] A. E. Phillips, G. J. Halder, K. W. Chapman, A. L. Goodwin, and C. J. Kepert, Zero thermal expansion in a flexible, stable framework: Tetramethylammonium copper(I) zinc(II) cyanide, J. Am. Chem. Soc. **132**, 10 (2010).

[19] J. R. Salvador, F. Guo, T. Hogan, and M. G. Kanatzidis, Zero thermal expansion in YbGaGe due to an electronic valence transition, Nature (London) **425**, 702 (2003).

[20] C. P. Romao, F. A. Perras, U. Werner-Zwanziger, J. A. Lussier, K. J. Miller, C. M. Calahoo, J. W. Zwanziger, M. Bieringer, B. A. Marinkovic, D. L. Bryce, and M. A. White, Zero thermal expansion in $ZrMgMo_3O_{12}$: NMR crystallography reveals origins of thermoelastic properties, Chem. Mater. **27**, 2633 (2015).

[21] J. Chen, X. Xing, C. Sun, P. Hu, R. Yu, X. Wang, and H. Li, Zero thermal expansion in $PbTiO_3$-based perovskites, J. Am. Chem. Soc. **130**, 1144 (2008).

[22] P. Hu, J. Chen, X. Sun, J. Deng, X. Chen, R. Yu, L. Qiao, and X. Xing, Zero thermal expansion in $(1-x)PbTiO_3$-xBi$(Mg, Ti)_{1/2}O_3$ piezoceramics, J. Mater. Chem. **19**, 1648 (2009).

[23] L. Hu, J. Chen, L. Fan, Y. Ren, Y. Rong, Z. Pan, J. Deng, R. Yu, and X. Xing, Zero thermal expansion and ferromagnetism in cubic $Sc_{1-x}M_xF_3$ (M = Ga, Fe) over a wide temperature range, J. Am. Chem. Soc. **136**, 13566 (2014).

[24] T. Wang, J. Xu, L. Hu, W. Wang, R. Huang, F. Han, Z. Pan, J. Deng, Y. Ren, L. Li, J. Chen, and X. Xing, Tunable thermal expansion and magnetism in Zr-doped ScF_3, Appl. Phys. Lett. **109**, 181901 (2016).

[25] I. Yamada, S. Marukawa, N. Hayashi, M. Matsushita, and T. Irifune, Room-temperature zero thermal expansion in a cubic perovskite oxide $SrCu_3Fe_{4-x}Mn_xO_{12}$, Appl. Phys. Lett. **106**, 151901 (2015).

[26] S. Li, R. Huang, Y. Zhao, W. Wang, Y. Han, and L. Li, Zero thermal expansion achieved by an electrolytic hydriding method in $La(Fe, Si)_{13}$ compounds, Adv. Funct. Mater. **27**, 1604195 (2017).

[27] Z. Ren, R. Zhao, X. Chen, M. Li, X. Li, H. Tian, Z. Zhang, and G. Han, Mesopores induced zero thermal expansion in single-crystal ferroelectrics, Nat. Commun. **9**, 1638 (2018).

[28] It is of course true that materials that have negative thermal expansion at low temperature and then positive thermal expansion at high temperature will have a range of intermediate temperatures where there is near-zero thermal expansion. Two examples where this occurs around room temperature or lower are silicon [65] and ZnS [66]. These cases occur because their phonons that cause the negative thermal expansion are at low frequencies, and the phonons that cause the more dominant positive thermal expansion are at a higher frequency, and the change in behavior on heating arises because only the lower frequency phonons are excited at low temperature, and the higher frequency phonons are only excited at higher temperatures. This is a different situation to that demonstrated in this paper, where we see a much tighter competition between both types of phonon and where the phonons that favor negative thermal expansion are not the lowest frequency modes.

[29] Y. Yang, X. Jiang, P. Gong, M. S. Molokeev, X. Li, Y. Li, X. Wu, Y. Wu, and Z. Lin, High mechanical strength in $Zn_4B_6O_{13}$ with an unique sodalite-cage structure, RSC Adv. **7**, 2038 (2017).

[30] Y. Liu, D. Mei, N. Wang, M. S. Molokeev, X. Jiang, and Z. Lin, Intrinsic isotropic near-zero thermal expansion in $Zn_4B_6O_{12}X$ (X = O, S, Se), ACS Appl. Mater. Interfaces **12**, 38435 (2020).

[31] H. Fang, M. T. Dove, L. H. N. Rimmer, and A. J. Misquitta, Simulation study of pressure and temperature dependence of

the negative thermal expansion in $Zn(CN)_2$, Phys. Rev. B **88**, 104306 (2013).

[32] M. T. Dove, J. Du, Z. Wei, D. A. Keen, M. G. Tucker, and A. E. Phillips, Quantitative understanding of negative thermal expansion in scandium trifluoride from neutron total scattering measurements, Phys. Rev. B **102**, 094105 (2020).

[33] P. Smith, S. Gaecia-Blanco, and L. Rivoir, The crystal structure of anhydrous zinc metaborate $Zn_4O(BO_2)_6$, Z. Kristallogr. **119**, 375 (1964).

[34] I. Hassan and H. D. Grundy, The crystal structures of sodalite-group minerals, Acta Crystallogr. Sect. B **40**, 6 (1984).

[35] D. Taylor and C. M. B. Henderson, A computer model for the cubic sodalite structure, Phys. Chem. Miner. **2**, 325 (1978).

[36] D. Hasha, L. Sierra de Saldarriaga, C. Saldarriaga, P. E. Hathaway, D. F. Cox, and M. E. Davis, Studies of silicoaluminophosphates with the sodalite structure, J. Am. Chem. Soc. **110**, 2127 (1988).

[37] K. D. Hammonds, M. T. Dove, A. P. Giddy, V. Heine, and B. Winkler, Rigid-unit phonon modes and structural phase transitions in framework silicates, Am. Mineral. **81**, 1057 (1996).

[38] K. D. Hammonds, H. Deng, V. Heine, and M. T. Dove, How Floppy Modes Give Rise to Adsorption Sites in Zeolites, Phys. Rev. Lett. **78**, 3701 (1997).

[39] K. D. Hammonds, V. Heine, and M. T. Dove, Rigid-unit modes and the quantitative determination of the flexibility possessed by zeolite frameworks, J. Phys. Chem. B **102**, 1759 (1998).

[40] J. Weitkamp, FUELS - HYDROGEN STORAGE | Zeolites, in *Encyclopedia of Electrochemical Power Sources* (Elsevier, Amsterdam, 2009), pp. 497–503.

[41] H. Fang and M. T. Dove, Pressure-induced softening as a common feature of framework structures with negative thermal expansion, Phys. Rev. B **87**, 214109 (2013).

[42] E. Grüneisen, Theorie des festen zustandes einatomiger elemente, Ann. Phys. **344**, 257 (1912).

[43] E. Grüneisen, Zustand des festen Körpers, in *Thermische Eigenschaften der Stoffe*, edited by C. Drucker, E. Grüneisen, P. Kohnstamm, F. Körber, K. Scheel, E. Schrödinger, F. Simon, J. D. van der Waals, and F. Henning (Springer, Berlin, 1926), Vol. 10, pp. 1–59.

[44] E. Grüneisen, The state of a solid body, NASA Technical Report **RE 2-18-59W**, 1 (1959).

[45] C. P. Romao, K. J. Miller, C. A. Whitman, M. A. White, and B. A. Marinkovic, Negative thermal expansion (thermomiotic) materials, in *Comprehensive Inorganic Chemistry II: From Elements to Applications* (Elsevier, Amsterdam, 2013), pp. 127–151.

[46] H. Fang, M. T. Dove, and A. E. Phillips, Common origin of negative thermal expansion and other exotic properties in ceramic and hybrid materials, Phys. Rev. B **89**, 214103 (2014).

[47] Y. Oba, T. Tadano, R. Akashi, and S. Tsuneyuki, First-principles study of phonon anharmonicity and negative thermal expansion in ScF_3, Phys. Rev. Materials **3**, 033601 (2019).

[48] S. Baroni, S. de Gironcoli, and A. D. Corso, Phonons and related crystal properties from density-functional perturbation theory, Rev. Mod. Phys. **73**, 515 (2001).

[49] K. Refson, P. R. Tulip, and S. J. Clark, Variational density-functional perturbation theory for dielectrics and lattice dynamics, Phys. Rev. B **73**, 155114 (2006).

[50] S. J. Clark, M. D. Segall, C. J. Pickard, P. J. Hasnip, M. I. J. Probert, K. Refson, and M. C. Payne, First principles methods using CASTEP, Z. Kristallogr. **220**, 567 (2005).

[51] J. P. Perdew, K. Burke, and M. Ernzerhof, Generalized Gradient Approximation Made Simple, Phys. Rev. Lett. **77**, 3865 (1996).

[52] J. P. Perdew, K. Burke, and M. Ernzerhof, Generalized Gradient Approximation Made Simple [Phys. Rev. Lett. **77**, 3865 (1996)], Phys. Rev. Lett. **78**, 1396 (1997).

[53] We prefer to use many random wave vectors within the first Brillouin zone rather than a regular grid in order to have confidence that the regular grid structure has no subtle effects on the results.

[54] L. H. N. Rimmer and M. T. Dove, Simulation study of negative thermal expansion in yttrium tungstate $Y_2W_3O_{12}$, J. Phys.: Condens. Matter **27**, 185401 (2015).

[55] L. H. N. Rimmer, M. T. Dove, A. L. Goodwin, and D. C. Palmer, Acoustic phonons and negative thermal expansion in MOF-5, Phys. Chem. Chem. Phys. **16**, 21144 (2014).

[56] L. H. N. Rimmer, M. T. Dove, B. Winkler, D. J. Wilson, K. Refson, and A. L. Goodwin, Framework flexibility and the negative thermal expansion mechanism of copper(I) oxide Cu_2O, Phys. Rev. B **89**, 214115 (2014).

[57] See Supplemental Material at http://link.aps.org/supplemental/10.1103/PhysRevB.104.174310 for Figs. S1 (IR and Raman spectra), S2 and S3 (phonon dispersion curves for $Zn_4B_6O_{12}S$ and $Zn_4B_6O_{12}Se$ respectively), S4 and S5 (mode decompositions for $Zn_4B_6O_{12}S$ and $Zn_4B_6O_{12}Se$ respectively) and S6 (graph of heat capacities), and Tabs. S1 and S2 (Calculated zone center phonon frequencies), and S3–S5 (tentative experimental zone center phonon frequencies).

[58] M. T. Dove, *Introduction to Lattice Dynamics* (Cambridge University Press, Cambridge, UK, 1993), Chap. 7.

[59] L. Elcoro and J. Etxebarria, Common misconceptions about the dynamical theory of crystal lattices: Cauchy relations, lattice potentials and infinite crystals, Eur. J. Phys. **32**, 25 (2010).

[60] A. P. Giddy, M. T. Dove, G. S. Pawley, and V. Heine, The determination of rigid-unit modes as potential soft modes for displacive phase transitions in framework crystal structures, Acta Crystallogr. Sect. A **49**, 697 (1993).

[61] J. W. Couves, R. H. Jones, S. C. Parker, P. Tschaufeser, and C. R. A. Catlow, Experimental verification of a predicted negative thermal expansivity of crystalline zeolites, J. Phys.: Condens. Matter **5**, L329 (1993).

[62] P. Tschaufeser and S. C. Parker, Thermal expansion behavior of zeolites and $AlPO_4$s, J. Phys. Chem. **99**, 10609 (1995).

[63] V. Heine, P. R. L. Welche, and M. T. Dove, Geometrical origin and theory of negative thermal expansion in framework structures, J. Am. Ceram. Soc. **82**, 1793 (1999).

[64] M. T. Dove, Flexibility of network materials and the Rigid Unit Mode model: A personal perspective, Philos. Trans. R. Soc. Ser. A **377**, 20180222 (2019).

[65] M. Ekman, K. Persson, and G. Grimvall, Lattice dynamics and thermodynamic properties of the β-Sn phase in Si, Phys. Rev. B **62**, 14784 (2000).

[66] S. Q. Wang, First-principles study of the anisotropic thermal expansion of wurtzite ZnS, Appl. Phys. Lett. **88**, 061902 (2006).